1 **Effect of far-infrared radiation assisted drying on microstructure of banana slices:**

2 **An illustrative use of X-ray microtomography in microstructural evaluation of a**

3 **food product**

4

5 **Angélique Léonard[1],[*], Silvia Blacher[1], Chatchai Nimmol[2], Sakamon Devahastin[3]**

6 [1]Laboratory of Chemical Engineering, Department of Applied Chemistry

7 University of Liège, FNRS, B6c, Sart Tilman, 4000 Liège, Belgium

8 [2]School of Energy, Environment and Materials, [3]Department of Food Engineering

9 King Mongkut's University of Technology Thonburi

10 126 Pracha u-tid Road, Bangkok 10140, Thailand

11

12 **Abstract**

13   X-ray microtomography coupled with image analysis represents a non-destructive technique,

14 which allows scanning an entire sample to obtain such information as total pore volume and pore size

15 distribution without the need of serial cuts as in the case of scanning electron microscopy (SEM). The

16 technique has been applied successfully to obtain reliable microstructural information of many products

17 undergoing different physical and chemical processes. However, the technique has still found limited

18 use in food processing. To illustrate the use of X-ray microtomography the technique was applied to

19 investigate the effect of far-infrared radiation (FIR) assisted drying on microstructure of a food product

20 viz. banana. Two representative drying techniques, i.e., low-pressure superheated steam drying

21 (LPSSD) and vacuum drying (VACUUM) were tested. Banana slices were dried by LPSSD-FIR at two

22 different temperatures (80 and 90°C) at a fixed pressure of 7 kPa. The total pore volume and pore size

23 distribution of dried banana slices were then determined using X-ray microtomography. The results

[*]Corresponding author. Tel.: +32 4 366 47 22; Fax: +32 4 366 28 18. E-mail: a.leonard@ulg.ac.be

24 were also compared with those of products dried by LPSSD without FIR. Far-infrared radiation was

25 found to modify the structure of the dried bananas by increasing their final porosity. The same effect of

26 FIR was also observed in the case of vacuum drying with FIR (VACUUM-FIR). An increase of the

27 drying temperature was also found to globally lead to an increase in the final porosity of the products.

28

29 Keywords: Image analysis; low-pressure superheated steam drying; microstructure; porosity; X-ray

30 microtomography; vacuum drying

31

32 **1. Introduction**

33   Although scanning electron microscopy (SEM) is a significant means to analyze the

34 microstructure of a sample, SEM does not give reliable information on the total pore volume and pore

35 size distribution of the sample. Indeed, due to the small parts that can be investigated with this method,

36 measurements must be largely repeated in order to give statistically relevant results. Moreover, this

37 technique fails to describe the whole 3D morphology as only 2D information is obtained. X-ray

38 microtomography, on the other hand, is a powerful technique that can be used to obtain the above

39 information. The main advantage of X-ray microtomography lies in its non-destructive character, as

40 opposed to SEM that requires cutting of the sample. With its large field of view, X-ray

41 microtomography also allows scanning of the entire sample. This technique is quite new in the field of

42 food engineering (van Dalen, Blonk, van Haalts, & Hendriks, 2003; Lim & Barigou, 2004; Haedelt,

43 Pyle, Beckett, & Niranjan, 2005; Babin, Della Valle, Chiron, Cloetens, Hoszowska, Pernot et al., 2006)

44 but it has been successfully applied for the characterization of highly porous materials (Léonard, Guiot,

45 Pirard, Crine, Balligand, & Blacher, 2007; Blacher, Calberg, Kerckhofs, Léonard, Wevers, Jérôme et

46 al., 2006; Blacher, Léonard, Heinrichs, Tcherkassova, Ferauche, Crine et al., 2004), the follow-up of

47 shrinkage and crack formation (Léonard, Blacher, Marchot, Pirard, & Crine, 2004; Job, Sabatier,

48 Pirard, Crine, & Léonard, 2006) as well as internal moisture profiles during drying (Léonard, Blacher,

49 Marchot, Pirard, & Crine, 2005).

50   Porosity is one of the important properties of dried foods and is generally related to their

51 texture. To obtain dried products with higher degree of porosity several novel drying methods have

52 been proposed and tested. Low-pressure superheated steam drying (LPSSD) is one of the drying

53 techniques that has recently been applied to various products for the above-mentioned purpose. Due to

54 the low-pressure environment and evolution of evaporated moisture within the products during LPSSD,

55 high-pressure gradients within the products occur, leading to an expansion of the cells of the products.

56 Consequently, LPSSD dried products have more porous structure than those obtained by conventional

57 hot air drying or vacuum drying (Devahastin, Suvarnakuta, Soponronnarit, & Mujumdar, 2004).

58 Despite the potential of LPSSD to provide dried products with higher degree of porosity, the process is

59 rather slow. To accelerate the drying process, a drying system combining LPSSD and far-infrared

60 radiation (FIR) has been developed and applied successfully to a heat-sensitive food material (Nimmol,

61 Devahastin, Swasdisevi, & Soponronnarit, 2007). It was found in this latter work that when FIR was

62 applied to the process as an additional heat source, not only the drying time was reduced but the dried

63 product quality, as assessed by texture analysis and SEM, was also improved.

64   As an illustrative example of the use of X-ray microtomography to evaluate the microstructure

65 of a food product undergoing drying, the effect of FIR on the microstructure of banana slices dried by

66 the system combining LPSSD and FIR (or LPSSD-FIR) was analysed. The results were also compared

67 with those obtained by only low-pressure superheated steam drying (LPSSD), vacuum drying

68 (VACUUM), and combination of FIR with vacuum drying (VACUUM-FIR). Two drying

69 temperatures, 80 and 90°C, were investigated in this work.

70

71

72

2. Experimental set-up, materials and methods

2.1. Experimental set-up

Fig. 1 shows a schematic diagram of the far-infrared radiation assisted drying system (Nimmol et al., 2007). Depending on whether the steam injection was switched on or off, two operating modes were respectively realized, i.e., low-pressure superheated steam drying or vacuum drying. The dryer consists mainly of a stainless steel drying chamber with inner dimensions of $45 \times 45 \times 45$ cm^3; a boiler for steam production; a steam reservoir, which maintained a steam pressure at around 200 kPa; a liquid ring vacuum pump (Nash, ET32030, Trumball, CT), which was used to maintain vacuum in the drying chamber; a sample holder; a load cell (Minebea, Ucg-3 kg, Nagano, Japan) with an accuracy of ± 0.2 g, which was used to record continuously the mass of the sample (at 1 min interval); a far-infrared radiator (Infrapara, A-2T-500, Selangor, Malaysia) rated at 500 W with a surface area of 60×120 mm^2, which was used to supply thermal radiation to the drying sample and the drying medium in the case of LPSSD-FIR and VACUUM-FIR experiments; and an electric heater rated at 1500 W, which was used to maintain the superheated steam and air temperature in the case of LPSSD and VACUUM experiments.

The operation of the far-infrared radiator was controlled through the temperature of the drying medium (air or superheated steam) measured at 30 mm above the sample surface via the use of a Proportional-Integral-Derivative (PID) controller (Shinko, JCS-33A-R/M, Osaka, Japan) with an accuracy of $\pm 0.1^{\circ}$C. Similar to the far-infrared radiator, the operation of the electric heater was also controlled by a PID controller (Omron, E5CN, Tokyo, Japan) with an accuracy of $\pm 0.1^{\circ}$C. The temperatures of the drying medium and of the drying sample were measured continuously using type K thermocouples. Thermocouple signals were multiplexed to a data acquisition card (Omega Engineering, CIO-DAS16Jr., Stamford, CT) installed in a PC. Labtech Notebook software (version 12.1, Laboratory Technologies Corp., Wilmington, MA) was then used to read and record the temperature data.

2.2. Material

98   Gros Michel banana (*Musa Sapientum* L.) was used as the tested material in this study. Fresh

99   banana with initial moisture content (AOAC, 1984) in the range of 2.65 to 3.10 kg/kg (d.b.) and

100   selected ripeness level of green tip (color index no. 5) was obtained from a local supermarket in

101   Bangkok, Thailand and stored at 4°C. Before each drying experiment, banana was peeled and sliced by

102   an electric food slicer (Chef's Choice, 667S, Aurora, NE) to 3 mm thick. The sliced samples were then

103   cut into 30 mm diameter using a die.

104

105   **2.3. Methods**

106   In this study, approximately 16 pieces of prepared banana slices were used in each drying

107   experiment. The experiments were carried out at the drying medium temperatures of 80 and 90°C and

108   absolute chamber pressure of 7 kPa. It should be noted that low-pressure superheated steam was the

109   drying medium in the case of LPSSD-FIR and LPSSD experiments, while low-pressure air was the

110   drying medium in the case of VACUUM-FIR and VACUUM experiments. Since the forced convection

111   in the drying chamber led to lower temperatures of the far-infrared radiator and of the samples leading

112   to lower drying rates, the electric fans were not used in the case of VACUUM-FIR experiments.

113   Detailed methods of LPSSD-FIR and VACUUM-FIR experiments can be found in Nimmol et al.

114   (2007), while detailed methods of LPSSD and VACUUM experiments are available in Devahastin et

115   al. (2004). The drying experiments were performed until a moisture content of 0.035 kg/kg (d.b.) was

116   obtained. This final moisture content was estimated from both the knowledge of the initial water

117   content and the loss of mass, obtained through the drying curve. All experiments were performed in

118   duplicate.

119

120   **2.4. X-ray microtomography**

121   X-ray microtomography is a powerful non-invasive technique allowing the visualization of the

122   internal structure of a sample based upon local variation of the X-ray attenuation coefficient. During

5

123   tomographic investigation an X-ray beam is sent to the sample and the transmitted beam is recorded by

124   a detector. According to the Beer-Lambert's law the transmitted intensity is related to the integral of the

125   X-ray attenuation coefficient (μ) along the path of the beam. This coefficient depends on the density

126   (ρ), the atomic number (Z) of the material and on the energy of the incident beam (E) according to

127   Equation (1):

128
$$\mu = \rho\left(a + \frac{bZ^{3.8}}{E^{3.2}} \right) \tag{1}$$

129   where a is a quantity with a relatively small energy dependence and b is a constant (Vinegar &

130   Wellington, 1987).

131   Projections (assembling of transmitted beams) are recorded for several angular positions by

132   rotating the sample between 0 and 180°. Then, a back-projection algorithm is used to reconstruct 2D or

133   3D images, depending on the method used. In the case of 2D images each pixel has a grey level value

134   corresponding to the local attenuation coefficient.

135   The "Skyscan-1172 high-resolution desk-top micro-CT system" (Skyscan, Kontich, Belgium)

136   was used in this study. A banana slice was placed vertically in a polystyrene holder, the latter being

137   almost transparent to X-rays. In contrast to a classical medical scanner, the source and the detector

138   were fixed, while the sample was rotated during the measurement. The cone beam source operated at

139   60 kV and 167 µA. The detector was 2D, 1048×2000 pixels, 16-bit X-ray camera. The distance source-

140   object-camera was adjusted to produce images with a pixel size of 15 µm. Because of the sample

141   height, three successive sub-scans, each corresponding to one third of the slice height, had to be

142   performed. The rotation step was fixed at 0.4°. For each angular position, a radiograph of the sample,

143   instead of a 1D-projection of a cross-section, was recorded by a 2D camera.

144   Fig. 2 shows a typical radiograph obtained after the three sub-scans were linked together. The

145   acquisition time required for each of the three segments was close to 50 minutes. The Feldcamp back

146   projection algorithm was used to reconstruct 2D images of the cross-sections. For each banana slice

147 about 200 cross-sections, separated by 150 μm, were reconstructed. Fig. 3a and b show typical grey

148 level cross-sections obtained for two vertical positions in the sample.

149

150 **2.5. Image analysis and measurement**

151   3D images of the samples were built by stacking ca. 200 cross sections obtained by X-ray

152 microtomography. The resulting 3D grey level images were formed by two phases: the pore space at

153 low grey levels (dark voxels), and the banana skeleton at high grey levels (bright voxels) (see Fig. 3a

154 and 3b). To perform a measurement the 3D image was preliminary segmented by assigning the value 1

155 to all pixels whose intensity was below a given grey tone value and 0 to the others, which implies

156 fixing a threshold on the 3D grey level image. This threshold was determined as follows: an automatic

157 threshold based on the entropy of the histogram (Sahoo, Soltani, Wong, & Chen, 1988) was calculated

158 for each 2D cross section. In this method, the inter-class entropy (S), defined by Equation (2), was

159 maximized.

160 $$S = -\sum p_i * \log(p_i) \tag{2}$$

161 where p_i is the probability of a pixel grey scale value in the image.

162   Figs 3c and 3d show the result of the segmentation process applied to Figs. 3a and 3b,

163 respectively. The threshold values obtained from the entropy method for the set of cross sections,

164 which formed each 3D image, were very close indicating that skeleton tomograms had a homogeneous

165 contrast. Then, a single threshold value for the 3D images was determined as an average of the cross

166 section thresholds. After this thresholding step, some small black holes were still present in the image

167 and were removed by applying a closing filter (Soille, 1999).

168   From the 3D processed binary images the porosity (δ), defined as the fraction of voxels of the

169 image that belong to the pores, was first measured. As the 3D images of banana slices presented a

170 continuous and rather disordered pore structure in which it was not possible to assign to each pore a

171 precise geometry, a standard granulometry measurement could not be applied. Therefore, to quantify

172 the larger pore sizes, the opening size distribution (Soille, 1999), which allows assigning a size to both

173 continuous and individual particles, was calculated. When an opening transformation was performed on

174 a binary image with a structuring element (SE) of size λ, the image was replaced by an envelope of all

175 SEs inscribed in its objects. For the sake of simplicity spheres of increasing radii λ (approximated by

176 octahedra) were used. When an image was opened by a sphere whose diameter was smaller than the

177 smallest features of its objects it remains unchanged. As the size of the sphere increased, larger parts of

178 the objects were removed by the opening transformation. Therefore, opening could be considered as

179 equivalent to a physical sieving process. This procedure was applied to the reversed 3D images of the

180 foams, i.e., to the 3D images in which pores correspond to white measurable voxels and the matrix to

181 black voxels. Image processing and measurements were performed with software Aphelion 3.2 (Adsis,

182 Meythet, France) on a PC.

183

184 **3. Results and discussion**

185 **3.1. Temperature evolution of banana slices during drying**

186 Because the temperature of the samples during drying is an important factor influencing their

187 pore structure, the temperature of banana slices undergoing different drying methods and conditions is

188 first discussed. As revealed by Figs. 4a and b the temperature of the samples undergoing the process

189 applying FIR (LPSSD-FIR and VACUUM-FIR) was much higher than that of samples undergoing

190 LPSSD and VACUUM. This is due to an extra heating. In the cases of LPSSD and LPSSD-FIR, the

191 periods of constant sample temperature, which were consistent with the period of constant drying rates,

192 were observed after a rapid increase of the sample temperature during the first 10 min of drying. For

193 LPSSD the level of constant sample temperature was the boiling point of water corresponding to the

194 chamber pressure. However, for LPSSD-FIR the level of constant sample temperature was higher than

195 the boiling point of water because FIR was present. For the processes without the application of

8

196   superheated steam (VACUUM and VACUUM-FIR) no periods of constant sample temperature were

197   observed because no constant drying rate periods were observed (Nimmol et al., 2007). It should also

198   be noted from Fig. 4 that the temperatures of LPSSD-FIR and VACUUM-FIR samples during the later

199   stages of drying rose to levels higher than the set medium temperatures and remained rather constant

200   until the end of the processes. This is again due to the influence of additional energy obtained from

201   FIR. These results are in contrast to those of LPSSD and VACUUM for which the sample temperature

202   approached the drying medium temperature toward the end of drying. It was also observed that the

203   sample temperature during the later stage of LPSSD-FIR was higher than that in the case of

204   VACUUM-FIR. This is because in the case of LPSSD-FIR the far-infrared radiator was used more

205   often due to the fact that the far-infrared absorptivity of superheated steam is higher than that of air

206   (Nimmol et al., 2007). More detailed explanation of the temperature evolutions during drying using

207   methods employed in this study is available in Nimmol et al. (2007) and Thomkapanish, Suvarnakuta,

208   & Devahastin (2007).

209

210   **3.2. Pore structure characterization**

211   The total porosity obtained from the 3D reconstructed images of banana slices are listed in

212   Table 1. The porosity values indicated that an increase in the drying temperature generally led to an

213   increase in the porosity of the samples. This is because drying at a higher temperature resulted in a

214   higher sample temperature and hence higher pressure gradients within the sample. These gradients in

215   turn led to stronger evolution of moisture within the sample during drying resulting in higher values of

216   the sample porosity.

217   At the same drying temperature, the use of FIR clearly resulted in an increase of the sample

218   porosity in all cases. For example, at 90°C a relative augmentation of about 32 and 37% was observed

219   in the case of LPSSD and VACUUM, respectively, when FIR was used. This is due to the fact that

220   during the processes applying FIR higher sample temperature was developed (see again Fig. 4).

9

221 Consequently, the internal pressure gradients increased more intensely leading to high-porosity

222 products. It is also found from Table 1 that drying at a higher temperature led to the dried products with

223 higher porosity in almost all cases, except for VACUUM. This may probably be due to the fact that, in

224 the case of VACUUM, the stresses developed during drying at a higher temperature were larger and

225 this led to a higher degree of microstructural deformation and collapse of structure leading to denser

226 structure of the product (Devahastin et al., 2004). No additional effect of FIR was also present to help

227 expanding the sample structure as well in the case of VACUUM.

228   It should be noted from Table 1 that when drying was performed at a higher temperature (90°C)

229 the porosity values of LPSSD and LPSSD-FIR samples were higher than those of VACUUM and

230 VACUUM-FIR samples, respectively. This is due to a rapid increase of the sample temperature during

231 initial stages of LPSSD and LPSSD-FIR (see Fig. 4b) resulting in rigorous boiling of moisture within

232 the samples. However, the results were opposite when drying was performed at a lower temperature

233 (80°C). This may probably be due to the effect of an inversion phenomenon (Suvarnakuta, Devahastin,

234 Soponronnarit, & Mujumdar, 2005), which happened somewhere between 80 and 90°C in this case

235 (Nimmol et al. 2007; Thomkapanish et al., 2007). This effect could also be viewed from the evolution

236 of the sample temperature. Although a rapid increase of the sample temperature during an initial stage

237 was also observed in the cases of LPSSD and LPSSD-FIR at 80°C, the period of constant sample

238 temperature occurring afterwards was clearly found to be longer than that at 90°C (see Fig.4a).

239 Consequently, moisture within the samples had less chance to boil rigorously leading to lower degrees

240 of porosity.

241   The observed changes of porosity could be attributed to a modification of the pore size

242 distribution. Figs. 5a and 5b show the histograms comparing the pore size distribution of the samples

243 obtained at 80 and 90°C with LPSSD and LPSSD-FIR, respectively. Figs. 6a and 6b show the

244 histograms representing the pore size distribution of the samples obtained at 90°C with LPSSD-FIR

245 and LPSSD as well as VACUUM-FIR and VACUUM, respectively. These four figures clearly show

246 that the pore sizes were non-normally distributed but that pores with sizes lower than 100 μm

247 prevailed. The use of FIR as well as a higher drying temperature resulted in a shift of the distribution

248 towards larger pore sizes for both drying techniques; the frequency of pores whose sizes were smaller

249 than 50 μm clearly decreased. Moreover, for LPSSD experiments, there was a frequency increase of

250 pores with sizes between 50 and 150 μm when the drying conditions were more intense, while for

251 VACUUM experiments large pores appeared, especially in the case of VACUUM-FIR for which pores

252 with diameters up to 450 μm were created.

253

254 **4. Conclusions**

255   X-ray microtomography coupled with 3D image analysis was used to study the effect of a

256 combination of far-infrared radiation (FIR) with low-pressure superheated steam drying or vacuum

257 drying. The results clearly showed that FIR and higher drying temperature led to an increase in the total

258 porosity and the displacement of pore size towards larger sizes. The knowledge of the pore structure is

259 essential in order to relate the quality of the product (e.g., shrinkage, rehydration and texture) to the

260 drying conditions and hence the ability to optimize the drying processes better.

261   Regarding its possibilities and advantages in comparison with classical characterization

262 techniques, X-ray microtomography will surely find a lot of applications in food engineering research.

263 It is important to note here, however, that this measurement was limited to micron-size pores although

264 submicron and even nano-size pores can be as important.

265

266 **Acknowledgements**

11

272 **References**

273 AOAC, (1984). *Official methods of analysis,* 14th edition, Association of Official Analytical Chemists,

274   Washington DC, USA.

275 Babin, P., Della Valle, G., Chiron, H., Cloetens, P., Hoszowska, J., Pernot, P., Reguerre, A.L., Salvo,

276   L., & Dendievel, R. (2006). Fast X-ray tomography analysis of bubble growth and foam setting

277   during breadmaking. *Journal of Cereal Science*, 43, 393-397.

278 Blacher, S., Calberg, C., Kerckhofs, G., Léonard, A., Wevers, M., Jérôme, R., & Pirard, J.P. (2006).

279   The porous structure of biodegradable scaffolds obtained with supercritical CO_2 as foaming

280   agent. *Studies in Surface Science and Catalysis*, 160, 681-688.

281 Blacher, S., Léonard, A., Heinrichs, B., Tcherkassova, N., Ferauche, F., Crine, M., Marchot, P.,

282   Loukine, E., & Pirard, J.P. (2004). Image analysis of X-ray microtomograms of Pd-Ag/SiO_2

283   xerogel catalysts supported on Al_2O_3 foams. *Colloids and Surfaces A: Physicochemical and*

284   *Engineering Aspects*, 241, 201-206.

285 Devahastin, S., Suvarnakuta, P., Soponronnarit, S., & Mujumdar, A.S. (2004). A comparative study of

286   low-pressure superheated steam and vacuum drying of a heat-sensitive material. *Drying*

287   *Technology*, 22, 1845-1867.

288 Haedelt, J., Pyle, D.L., Beckett, S.T., & Niranjan, K. (2005). Vacuum-induced bubble formation in

289   liquid-tempered chocolate. *Journal of Food Science*, 70, E159-E164.

290 Job, N., Sabatier, F., Pirard, J.P., Crine, M., & Léonard, A. (2006). Towards the production of carbon

291   xerogel monoliths by optimizing convective drying conditions. *Carbon*, 44, 2534-2542.

292   Léonard, A., Blacher, S., Marchot, P., Pirard, J.P., & Crine, M. (2004). Measurement of shrinkage and

293   cracks associated to convective drying of soft materials by X-ray microtomography. *Drying*

294   *Technology*, 22, 1695-1708.

295   Léonard, A., Blacher, S., Marchot, P., Pirard, J.P., & Crine, M. (2005). Moisture profiles determination

296   during convective drying using X-ray microtomography. *Canadian Journal of Chemical*

297   *Engineering*, 83, 127-131.

298   Léonard, A., Guiot, L., Pirard, J. P., Crine, M., Balligand, M., & Blacher, S. (2007). Non-destructive

299   characterization of deer antlers by X-ray microtomography coupled with image analysis.

300   *Journal of Microscopy,* 225, 258-263.

301   Lim, K.S. & Barigou, M. (2004). X-ray micro-computed tomography of cellular food products. *Food*

302   *Research International*, 37, 1001-1012.

303   Nimmol, C., Devahastin, S., Swasdisevi, T., & Soponronnarit, S. (2007). Drying of banana slices using

304   combined low-pressure superheated steam and far-infrared radiation. *Journal of Food*

305   *Engineering*, 81, 624-633.

306   Sahoo, P.K., Soltani, S., Wong, K.C., & Chen, Y.C. (1988). A survey of thresholding techniques.

307   *Computer Vision, Graphics, and Image Processing*, 41, 233-260.

308   Soille, P. (1999). *Morphological Image Analysis-Principles and Applications*. Springer-Verlag, New

309   York.

310   Suvarnakuta, P., Devahastin, S., Soponronnarit, S., & Mujumdar, A.S. (2005). Drying kinetics and

311   inversion temperature in a low-pressure superheated steam-drying system. *Industrial &*

312   *Engineering Chemistry Research,* 44, 1934-1941.

313   Thomkapanish, O., Suvarnakuta, P., & Devahastin, S. (2006). Study of intermittent low-pressure

314   superheated steam and vacuum drying of banana. *Drying Technology*, 25, 205-223.

315   van Dalen, G., Blonk, H., van Haalts, H., & Hendriks, C.L. (2003). 3-D imaging of foods using X-ray

316   microtomography. *G. I. T. Imaging & Microscopy*, 3, 18-21.

317   Vinegar, H.J. & Wellington, S.L. (1987). Tomographic imaging of three-phase flow experiments.

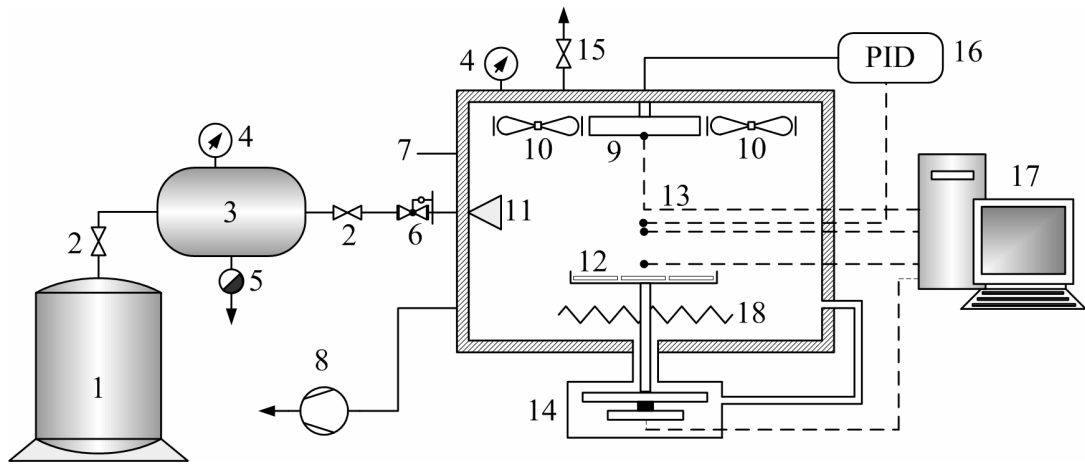318   *Review of Scientific Instruments*, 58, 96-107.

Fig. 1. A schematic diagram of the far-infrared radiation assisted drying system: 1) boiler; 2) steam valve; 3) steam reservoir; 4) pressure gauge; 5) steam trap; 6) steam regulator; 7) drying chamber; 8) vacuum pump; 9) far-infrared radiator; 10) electric fans; 11) steam inlet and distributor; 12) sample holder; 13) thermocouples; 14) load cell; 15); vacuum break-up valve; 16) PID controller; 17) PC with data acquisition card; 18) electric heater.
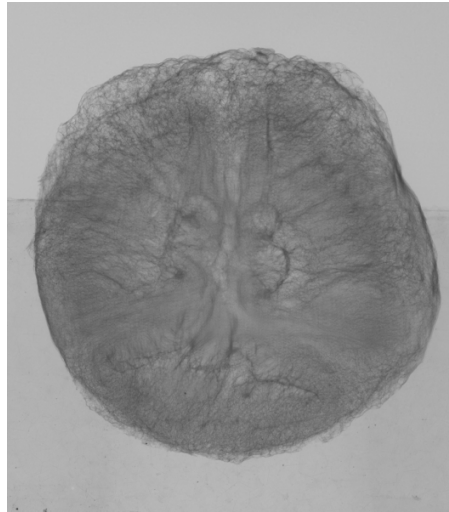
Fig. 2. Typical radiograph of a dried banana slice.
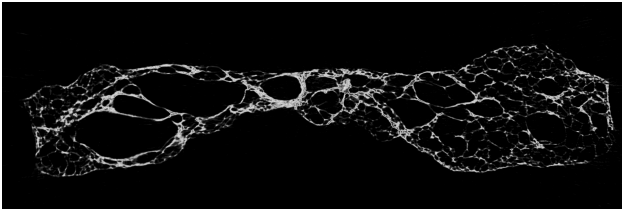
a)
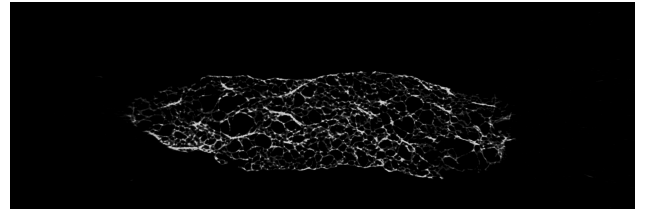
b)
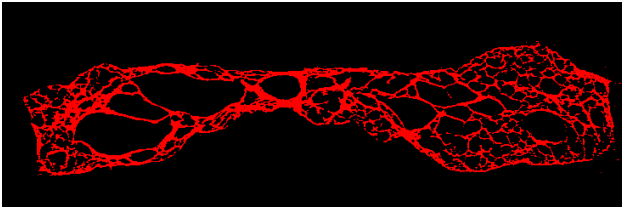
c)
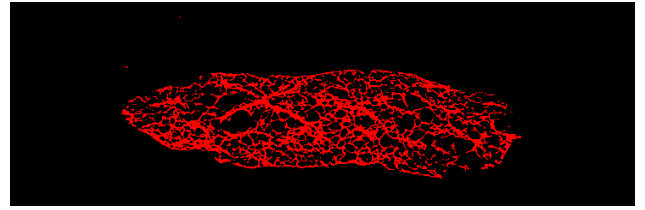
d)

Fig. 3. Grey level cross sections (a-b) and the corresponding binary images after thresholding (c-d).
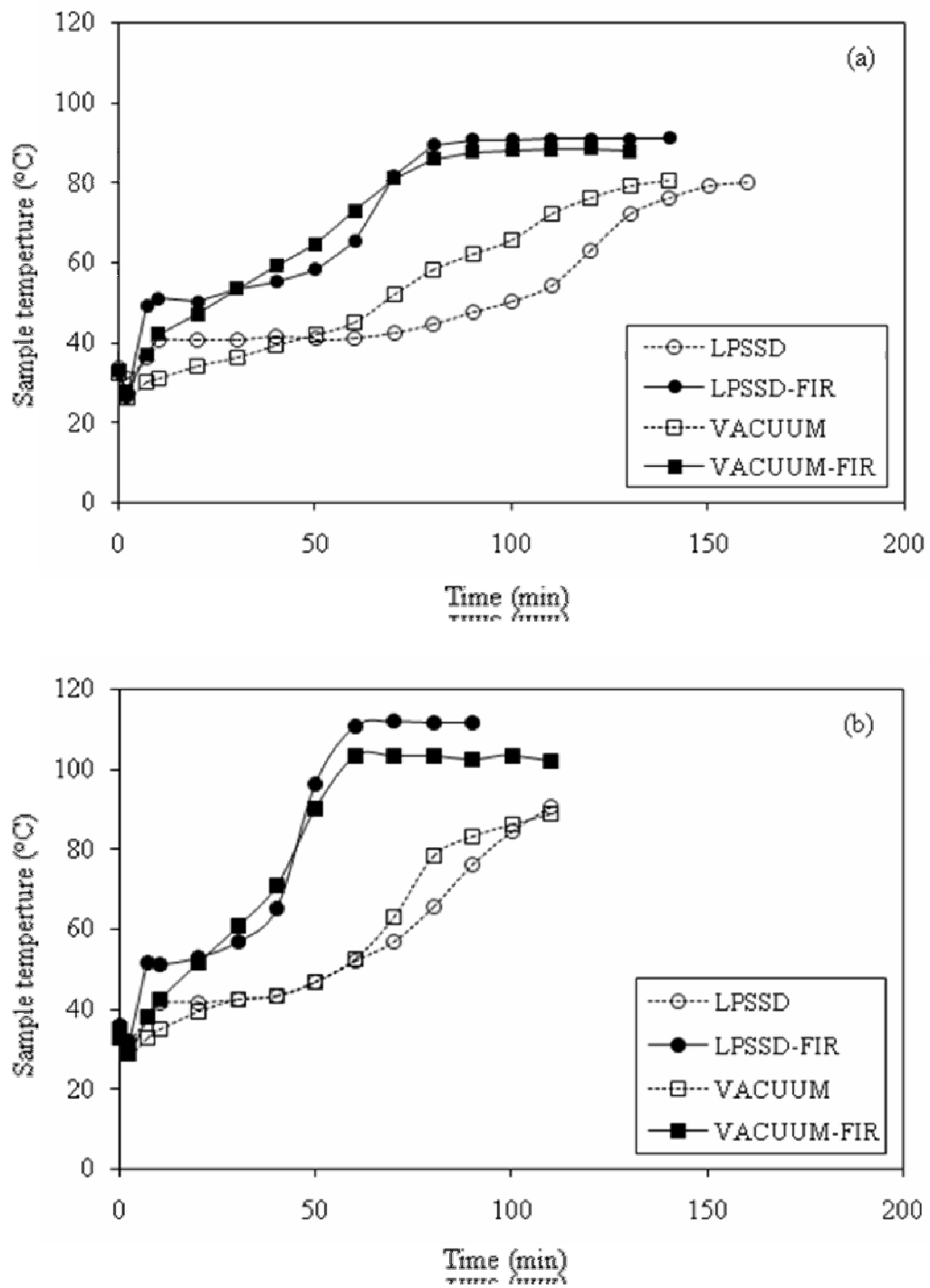
Fig. 4. Temperature evolution of banana slices dried at (a) $80^{\circ}C$ and (b) $90^{\circ}C$.
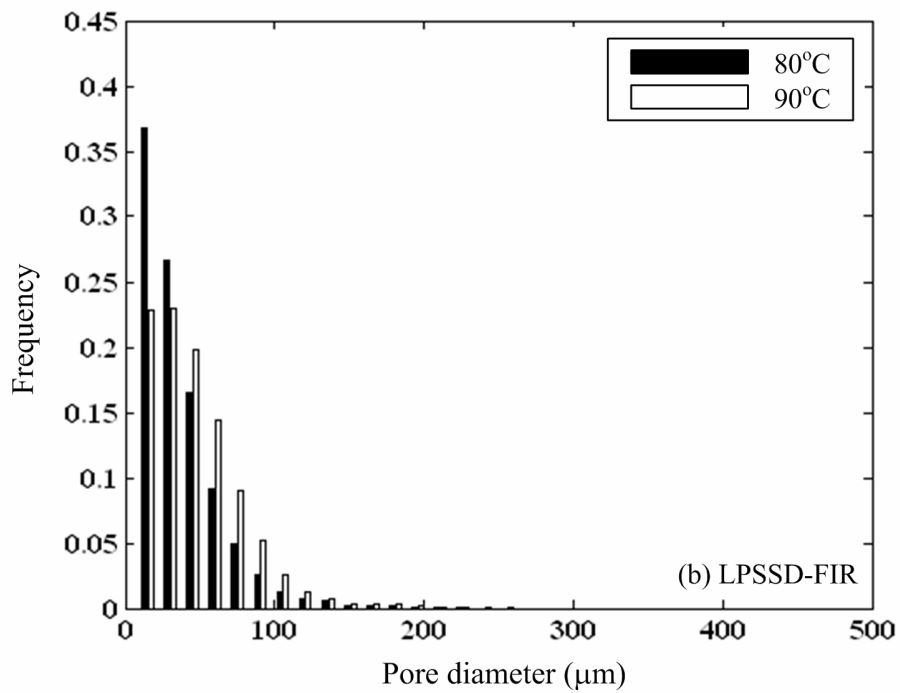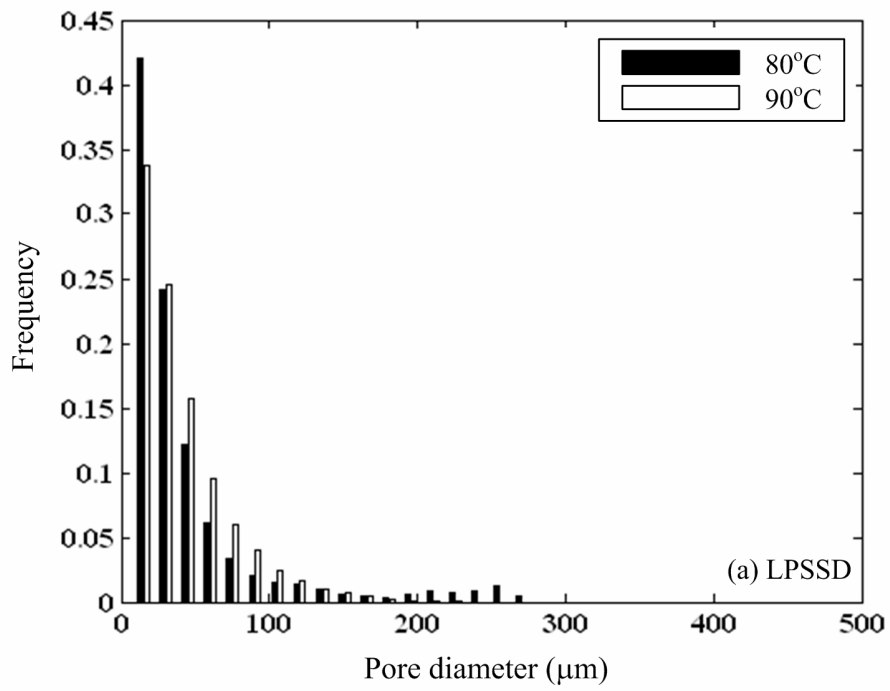
Fig. 5. Pore size distributions of the samples dried at 80 and 90°C with (a) LPSSD and (b) LPSSD-FIR.
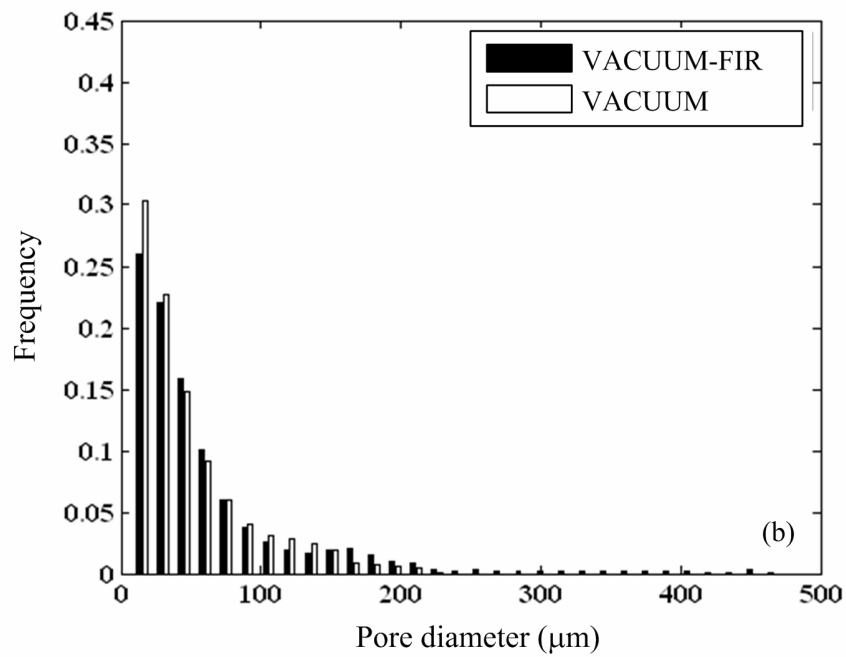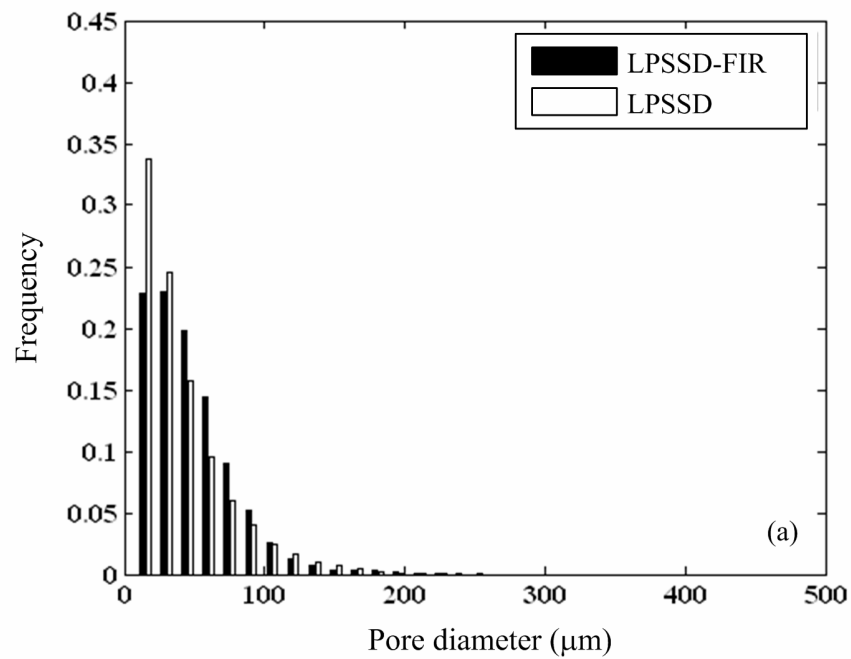
Fig. 6. Pore size distributions of the samples dried at 90°C.

(a) Comparison between LPSSD-FIR and LPSSD dried samples

(b) Comparison between VACUUM-FIR and VACUUM dried samples

Table 1 Total porosity of banana slices undergoing various drying methods at different drying conditions

Drying method	Drying temperature (°C)	Porosity
LPSSD	80	0.42±0.05
	90	0.53±0.06
LPSSD-FIR	80	0.55±0.06
	90	0.70±0.08
VACUUM	80	0.54±0.05
	90	0.46±0.05
VACUUM-FIR	80	0.57±0.06
	90	0.63±0.07